AIAA SciTech Forum
23-27 January 2023, National Harbor, MD & Online
AIAA SCITECH 2023 Forum

10.2514/6.2023-2025

Reconstruction of Tricalcium Silicate Microstructures for Repeating Unit Cell Analysis

Vishnu Saseendran[1], and Namiko Yamamoto[2]
Department of Aerospace Engineering, The Pennsylvania State University, University Park, PA, 16802 United States

Peter J. Collins[3], and Aleksandra Radlińska[4]
Department of Civil and Environmental Engineering, The Pennsylvania State University, University Park, PA, 16802 United States

Evan J. Pineda[5], and Brett A. Bednarcyk[6]
NASA Glenn Research Center, Cleveland, Ohio, 44135 United States

To realize large-scale habitats in extraterrestrial bodies, cement-like binders may be utilized along with in-situ materials such as lunar regolith. The hydration and morphology of cementitious systems formed in microgravity are not well understood. Previously, the size and morphology of a common cement binder was formed by hydration in the microgravity environment (10^{-6} or μg) aboard the International Space Station (ISS). Upon return to the ground, their micro-structures, including phase size and distribution, were visually inspected using scanning electron microscopy (SEM), in comparison with those of the samples hydrated on the ground in terrestrial gravity (1*g*). The sample hydrated in the μg environment showed larger porosity and larger calcium hydroxide (CH) crystals; air bubbles are trapped due to the lack of buoyancy, and CH crystals grew to fill in those pores. While the microstructures are well documented, their mechanical characterization has been a challenge due to size limitations and high porosity. Thus, in this study, such mechanical properties will be estimated using micromechanics-based modeling with the NASA Multiscale Analysis Tool (NASMAT). Micromechanics-based modeling requires 3D Repeating Unit Cell (RUCs) when used with highly porous samples. Representative 3D volumes for modeling are being constructed from the backscattered SEM images of the samples, available on NASA's Physical Sciences Informatics database, using a deep learning-based sub-volume reconstruction. This reconstruction method successfully captured the unique microstructural development (phase composition and morphology) of high water-to-cement ratio tricalcium silicate (C_3S) paste, which is the main mineral component of commercial Portland cement. The reconstructed volume was compared with a micro-CT scan of the samples. The reconstructed sub-volumes

[1] Postdoctoral Scholar, Department of Aerospace Engineering, The Pennsylvania State University. AIAA Member
[2] Associate Professor, Department of Aerospace Engineering, The Pennsylvania State University. AIAA Senior Member.
[3] Ph.D. Candidate, Department of Civil and Environmental Engineering, The Pennsylvania State University.
[4] Associate Professor, Department of Civil and Environmental Engineering, The Pennsylvania State University.
[5] Research Aerospace Engineer, NASA Glenn Multiscale and Multiphysics Modeling Branch, AIAA Senior Member.
[6] Research Aerospace Engineer, NASA Glenn Multiscale and Multiphysics Modeling Branch, AIAA Associate Fellow.

are then utilized as RUC in the NASMAT code. The workflow presented here can be applied to other multi-phase materials, beyond the space cement.

I. Introduction

With the advent of crewed missions, such as the Artemis program, there is a rejuvenated interest to prolong human space exploration missions. Invariably, to achieve this goal, there is a need to build habitats on extraterrestrial bodies such as the Moon and Mars, wherein, the gravitational force is significantly less than that of the Earth. In addition, given the cost of transporting materials into space, it is envisioned that *in situ* materials such as the lunar regolith will be used for the construction of habitats with the aid of cement-like binders. However, the solidification of these cement binders is not very well understood under the influence of microgravity (10^{-6} *g* or μ*g*). Previously, under the ambit of the project titled – "Microgravity Investigation of Cement Solidification (MICS)", common cement binder formations in the microgravity environment were studied [1,2]. In particular, tricalcium silicate (Ca_3SiO_5: C_3S in cement notation) and tricalcium aluminate ($Ca_3Al_2O_6$: C_3A in cement notation) were analyzed under both terrestrial (1*g*) as well as μ*g* conditions. Studying pure compounds, such as C_3S, aids in understanding the basic nature of microstructural formation in the μ*g* environment. Moreover, from the perspective of mechanical characterization and analysis, a thorough characterization of pure phases helps to make the workflow robust, prior to analyzing complex systems comprising other compounds such as aluminates, sulfates, alkalis, and other impurities. Moreover, such analyses will pave the way in establishing process-structure-property relationships of such compounds in microgravity conditions.

In μ*g* environment, due to the lack of buoyancy, the microstructure formation is predominantly influenced by air bubbles that remain intermixed with the cement paste. The porosity formation was well documented in [1] and is one order of magnitude larger than 1*g* for a high water-to-cement ratio mixture. Primarily, the hydration of C_3S leads to the formation of two distinct phases – C-S-H and CH (portlandite). Note that the usual cement chemistry notation is used throughout this manuscript, where C = CaO, S = SiO_2, and H = H_2O. The SEM images of both 1*g* and μ*g* samples clearly showcased these phase formations as well as the porosity (see **Figure 1**). It was reported that the porosity in the space-returned samples was over 20 percent larger compared to the 1*g* samples [1]. Moreover, the SEM images illustrate the significant differences between the microstructural formations. For instance, in the μ*g* sample, the portlandite (CH) phase exhibits larger and less frequent distribution in the C-S-H matrix. The major challenge for mechanical characterization pertaining to C_3S samples is their size limitation (rendering it difficult for conventional mechanical testing such as compression or 3-point bend) and high porous nature (difficult for microindentation). Therefore, micromechanics-based modeling is relied on here to perform mechanical characterization of both 1*g* and μ*g* hydrated C_3S samples. The micromechanics model High-Fidelity Generalized Method of Cells (HFGMC) in the NASA Multiscale Analysis Tool (NASMAT) will be used to obtain the mechanical response, including effective properties, and local stress and strain fields.

The success of a micromechanics-based analysis of a multi-phase material system depends on accurately describing individual phases (volume fraction, size, and morphology) in the repeating unit cell (RUC). Moreover, from the SEM image of the μ*g* sample, it is noted that in the absence of gravity, a larger prismatic morphology of CH crystallite is evident (refer to **Figure 1**). The 2D SEM images taken on polished surfaces of the hydrated C_3S samples can be transformed as microstructure input for the NASMAT code. However, as demonstrated in this work, this is an oversimplified assumption leading to inaccurate results. For robust analysis, the morphology of the CH crystals formed in space must be accurately represented using a 3D RUC in the micromechanics-based modeling approach. This can be achieved either with the aid of microtomography (micro-CT) or using an inverse numerical approach. The former is expensive due to the time and cost involved and the latter involves algorithms that reconstruct 3D microstructure from orthogonal 2D sectional slices [4, 5]. The 2D surface images can be easily obtained using optical methods such as optical microscopy or SEM. Hence, with the aid of a micromechanics-based approach, effective properties of the multi-phase system such as cementitious materials may be obtained using a statistical framework by building statistically equivalent 3D microstructures from the 2D sectional slices. Alternatively, the complex process of C_3S hydration can be readily analyzed using a number of existing codes in the field of cementitious materials, such as CEMHYD3D [6], HydratiCA [7], HYMOSTRUC [8] and μIC [9]. In general, these codes model chemical kinetics and capture both geometrical and topological properties of the microstructure with the aid of the autocorrelation function. The hydrating cement is modeled as gradually growing spheres with porosity typically described using an overlap algorithm.

In this study, high-quality 3D microstructures of both 1*g* and µg hydrated C_3S samples are generated using a solid texture synthesis approach based on a deep learning framework. In particular, the Convolutional Neural Networks (CNN) based model proposed by Gutierrez et al. [10] was utilized. The methodology showed promising results in the reconstruction of 3D microstructures using 2D SEM images of both 1*g* and µ*g* hydrated C_3S samples as input. The reconstructed sub-volumes were segmented using a histogram-based approach and will be transformed and discretized for 3D microstructure input in the NASMAT code. By aptly describing the plate-like morphology of portlandite crystals found in hydrated C_3S µg sample [refer to **Figure 1(b)**], the workflow presented here paves the way in simulating the mechanical response of cement binders in microgravity. In addition, complex loading conditions such as combined mechanical and thermal loading may be explored.

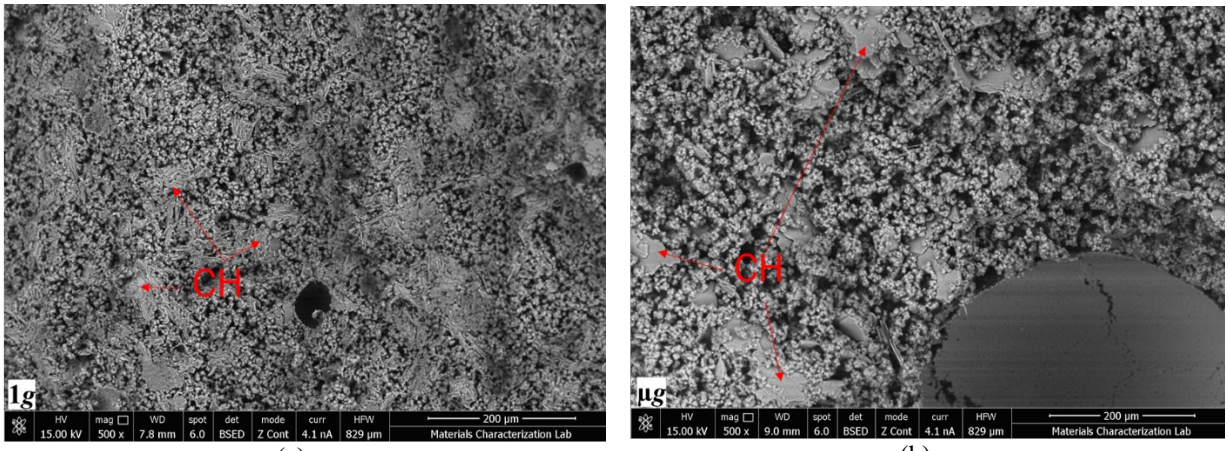

(a) (b)

Fig 1. Fractured surface of hydrated C_3S samples (a)1*g*, and (b) µ*g* conditions. The size and morphology of portlandite (C-H) crystals varies between 1*g* and *µ*g sample.

II. Sample Preparation and Image Analysis

The fabrication details of these samples can be found elsewhere [1]. The tricalcium silicate, C_3S, evaluated in this work was cured with lime water at a water-to-cement ratio (w/c) of 2.0 by mass. The high w/c ratio enhanced crystal growth by coarsening the porosity. Moreover, magnifying the effect of overall microstructural development aids in understanding the µ*g* effects. Pure water in place of lime water in a high w/c system will lead to an unrealistic rapid initial reaction. Whereas limewater controls the initial reaction rate and enhances initial nucleation and crystal growth [1]. The mixture constituents were held in commercially available plastic bags with burstable seals and the setup allowed the first contact between the C_3S and lime water to be onboard the ISS. Both space and ground samples were mixed simultaneously by exerting pressure on the lime-water compartment at the same conditions (20 ± 2 °C, 1 ATM, and 35% RH) such that the seal burst and allowed the solution to come in contact with the anhydrous C_3S. Note that gravity is assumed to be the only variable between space and ground experiments. Both processed ground and space samples remained within the sealed pouch for the entire hydration period undisturbed. The µ*g* samples were allowed to hydrate onboard the ISS for 42 days until returning to Earth. The retrieved samples were stored in insulated containers prior to analysis (for more details on analysis techniques, see [1]). The fractured surfaces of both µ*g* (shortly after returning, as well as 1g samples, were examined using Scanning Electron Microscopy (SEM). In addition, samples were dried under a vacuum, mounted in acrylic resin and polished. The Backscattered Electron (BSE) images of the polished sections were taken with a magnification of 500x and analyzed. In this work, the BSE images of both 1g and µ*g* samples saved in the NASA Physical Sciences Informatics (PSI) database are utilized.

A. Greyscale-based Image Segmentation

In both sample types, the BSE images showed large amount of porosity along with hydration products of the C_3S paste – CH crystals encapsulated in C-S-H matrix. The porosity was high in samples cured in space. The 1536 x 1024 pixels

BSE images had a resolution of 0.54 x 0.54 µm per pixel (a total of 20 µ*g* images and 19 1*g* images were considered). To identify phases, each image was segmented using the workflow shown in **Figure 2**. Due to the difference in atomic number, Z, of individual constituent phases, the histogram provides distinct peaks corresponding to each phase (see **Figure 3(a)**). However, to reliably identify each phase where the greyscale value is usually < 100, it was decided to modify the histogram. Firstly, the histogram was equalized (with 0.3% saturated pixels) which enhanced the contrast, followed by applying a Sigma filter [11]. Sigma filter has been proven to be successful in image analysis in cementitious systems such as identifying interfacial transition zone (ITZ) between cement paste and aggregates in concrete [12]. Here, the Sigma filter (with $\sigma = 2.0$) was applied after histogram equalization; the modified histogram with identified phase boundaries is shown in the plot [see **Figure 3(b)**]. The local minima approach was used to identify the bounds between each phase.

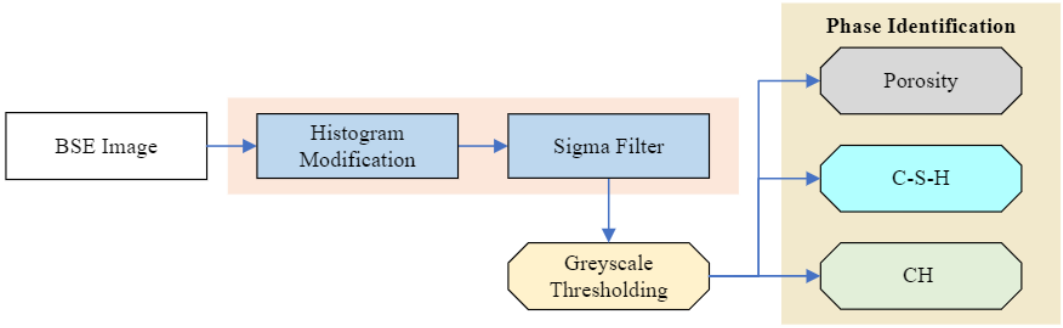

Fig 2. Greyscale-based BSE image segmentation workflow to identify each phase in hydrated C_3S samples.

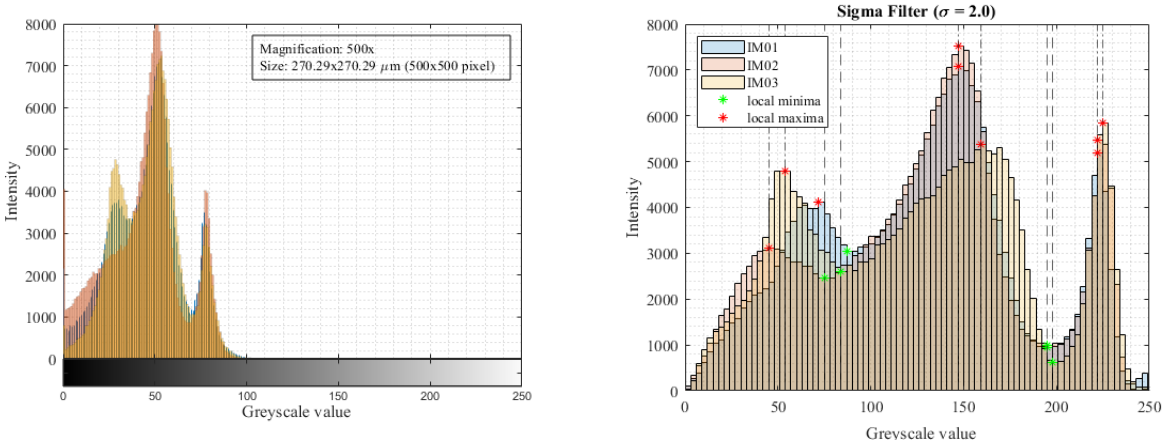

(a) (b)

Fig 3. Histogram equalization of BSE image and identified local minima-based bounds of 1*g* sample (a) original histogram (greyscale ~ <100) of a BSE image (500x500 pixels, 270.29x270.29 µm), and (b) identification of phases using the local minima approach after histogram equalization and sigma filter application.

As noted, the variation in the atomic number of individual phases results in distinct peaks in the histogram. However, at the phase boundary, edge effects can occur, especially when the discrepancy between the adjacent phases with respect to atomic number is larger. Moreover, such effects may be pronounced due to phase geometry, in particular, if the boundary is inclined towards the material with a lower atomic number, as is the case with porosity [12, 13]. To circumvent this issue, the boundary between porosity and the C-S-H phase in this research was identified using an approach widely employed in the cementitious materials – overflow method [14]. In this approach, the inflection point between the two phases is identified from a cumulative distribution plot [see **Figure 4(a)**]. The influence of this approach over the local minima is evident in the histogram plot provided in **Figure 4(b)**. It can be noted that the

Porosity/C-S-H bound increased from 78 to 115 when the overflow method is employed. The computed porosity content was recorded as 46.05 % instead of 27.64 % using the local-minima approach. Thus, the overflow method coupled with the local-minima approach was used to identify the Porosity/C-S-H and C-S-H/CH bounds and ascertain respective phase composition in the BSE images. **Table 1** provides the averaged area fraction of each constituent in both 1*g* and μ*g* samples taken from the NASA PSI database, and **Figure 5** shows the phase assignment visualized using color codes. Porosity assessment of both 1*g* and μ*g* samples was conducted using the Mercury Intrusion Porosimetry (MIP) technique and the results showed good agreement with the image analysis (refer to **Table 1**).

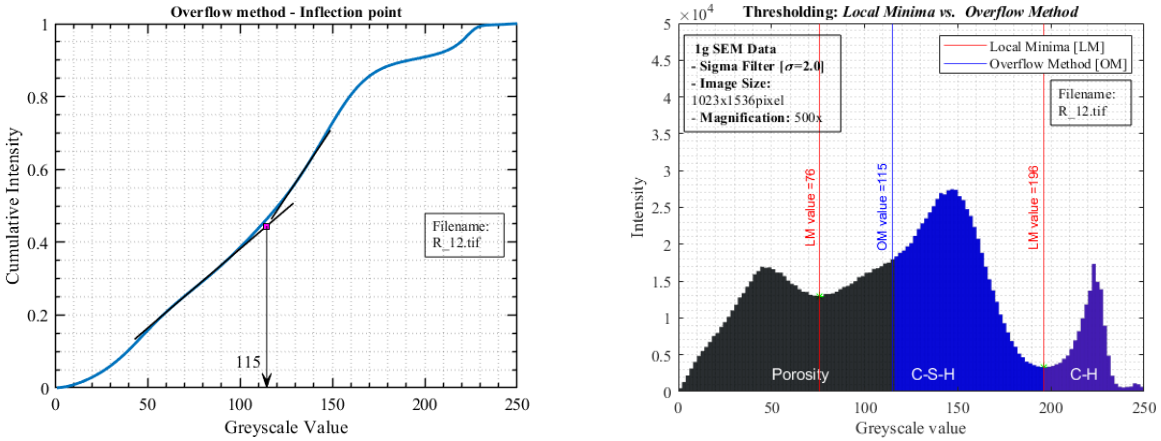

Fig 4. Inflection point and phase composition analysis from a modified histogram [equalization and sigma filter; σ = 2.0] of BSE image (500x500 pixels, 270.29x270.29 μm); C_3S sample hydrated on ground (1*g* sample) a) inflection point identified in the cumulative intensity plot, and (b) comparison of bounds at the porosity/C-S-H boundary obtained using overflow and local minima methods.

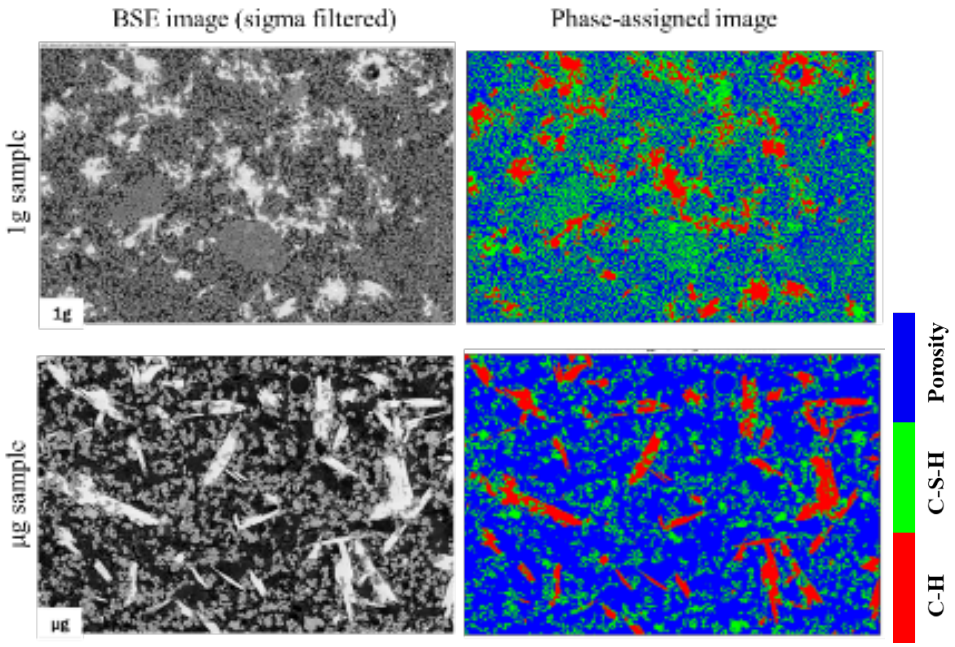

Fig 5. Visualization of phase assignment (1536x1021 pixels) in a C_3S sample hydrated on ground (1*g* sample, top) and in the microgravity (μ*g* sample, bottom); images were modified using histogram equalization followed by sigma filter application, and phase assignment using the overflow and local minima approach.

Table 1. Summary of individual phase composition obtained from image analysis.

	Porosity	C-S-H	CH
1*g* Samples	47.0 % ± 14.2 %	41.6 % ± 12.0 %	11.3 % ± 2.8 %
1*g* Samples MIP	48.4 %	-	-
μ*g* Samples	70.3 % ± 1.4 %	21.2 % ± 1.2 %	8.5 % ± 1.4 %
μ*g* Samples MIP	69.4 %	-	-

III. Convolutional Neural Network (CNN) -based Reconstruction of 3D Cement Microstructures

A. 2D Analysis in NASMAT

The phase-assigned, pixelated 2D images (refer to **Figure 5**) can be directly inputted into the NASMAT tool to assess effective stiffness properties and local stress/strain response. A standard linear elastic model was considered for each phase. A pilot study was conducted in NASMAT by using a 256 x 256 pixel [138 μm^2] user-defined doubly-periodic architecture as shown in **Figure 5**. A doubly-periodic RUC was constructed assuming each subcell in the RUC corresponded to a pixel in the image and was occupied by the appropriate constituent. Effective properties of the RUC were calculated via homogenization using the HFGMC micromechanics theory in NASMAT. However, as highlighted above, due to the high porosity content the 2D BSE image does not statistically represent the 3D microstructure of the hydrated cement. The doubly periodic analysis is presented here to demonstrate this.

The material properties of individual phases (C-S-H and CH) were taken from the literature, where the reported values are obtained using a nanoindentation study and assumed to be isotropic. The Young's modulus and Poisson's ratio of the C-S-H phase were assigned 21.7 GPa and 0.25, respectively. For the CH crystals, Young's modulus 40 GPa and Poisson's ratio 0.31 was assigned. **Figure 6** shows the stress-strain response of both 1*g* and μ*g* samples for a 1% compressive strain loading. Note that the measured porosity content in both 1*g* and μ*g* samples is 48.4 % and 69.4 %, respectively. HFGMC does not support open geometry. So, for the pilot study conducted here, the Young's modulus of the subcells occupying the porous space was varied; 1 MPa and 0.1 MPa were assumed which yielded Young's moduli of 233.1 MPa and 2083.3 MPa, respectively for the 1*g* sample. In the case of the μ*g* sample, the homogenized stiffness constants were 190.4 MPa and 1737.5 MPa when the Young's modulus of the subcells representing the porosity was 1 MPa and 0.1 MPa, respectively.

This obtained Young's modulus value in this doubly-periodic analysis drastically differed from the reported value for C_3S samples hydrated on the ground (typically in the range of 125 – 150 GPa). Therefore, analysis must be performed using a user-defined triply-periodic RUC that accurately captures the microstructure of hydrated C_3S samples. Here, the 3D microstructures of both 1*g* and μ*g* samples are reconstructed using a deep learning framework, and those results are discussed in the subsequent section.

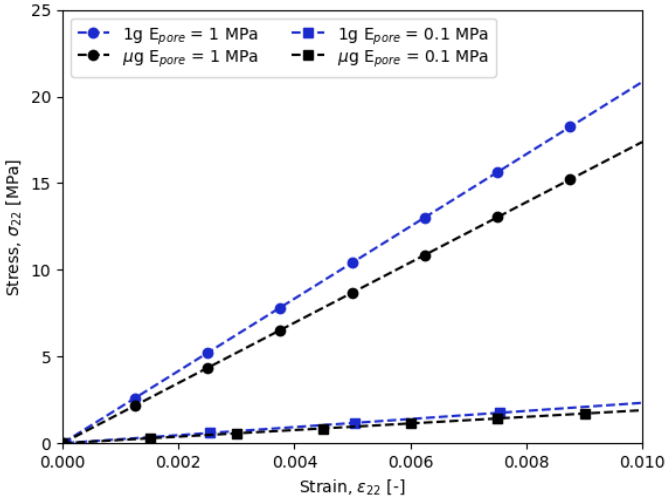

Fig 6. Global stress-strain response of 1g and µg sample for an applied 1 % strain loading.

B. Deep learning-based Reconstruction Algorithm

In the codes that simulate hydration of cementitious materials (refer to section I), autocorrelation-based functions are often used to model the microstructure with the aid of Particle Size Distribution (PSD). However, cement binders hydrated in space will result in portlandite crystals that have distinct plate-like morphology (see **Figure 1** and **Figure 5**). In any numerical-based simulation involving µg samples, this distinct morphology formed due to the lack of buoyancy must be sufficiently represented. Microstructure reconstruction techniques are becoming widely popular owing to their low cost and time compared to experimental characterization techniques that result in a limited number of sub-volumes in the sample. Moreover, for statistical convolution in establishing the process-structure-property relationship, a large ensemble of sub-volumes that represent the microstructure adequately is desired.

Amongst the microstructure reconstruction techniques, Markov Random Field (MRF) and machine learning-based techniques have received wide attention in recent years [4,5,15-19]. In the field of computer graphics, a certain set of algorithms have been developed recently that are similar to microstructure reconstruction. This technique, referred to as solid texture synthesis [15], has received wide attention and has been widely utilized to reconstruct realistic 3D images from 2D images (known as exemplars). In the literature, one of the most computationally effective solid texture synthesis algorithms is presented by Kopf et al. [16], wherein, a set of three images is used as input and provides a solid texture as output. The output is generated based on a search and optimization step that minimizes the error amongst the best-matching neighborhoods. The input images can be 2D slices from any orthogonal direction, or a series of slices in any particular direction. More recently, a compact solid texture generator model based on Convolutional Neural Networks (CNN) was proposed by Gutierrez et al. [17]. In this model, a pre-trained deep learning model - VGG19 [18] is utilized, and the volumetric loss function of the generated 2D slices is compared to the input 2D exemplar using a perpetual loss function. In addition, this methodology is fast and computationally efficient as only the 2D slices are generated during the training stage. This framework was adapted in our study to reconstruct the microstructure of both 1*g* and µ*g* samples. The reconstructed microstructure can be directly implemented in NASMAT as a user-defined triply-periodic RUC.

The model framework employed here, shown in **Figure 7,** consists of the generator and descriptor. More recently, this same algorithm was shown to successfully generate high-quality 3D microstructures of hardened cement [19]. Note that the pre-trained model used here, VGG19, is trained on ImageNet [20] which includes a very diverse set of images under various imaging conditions. VGG19 has a total of 16 convolutional layers and 5 pooling layers (divided into 5 blocks). It accepts a 2D image with a 3-channel (RGB) as input. Hence, the two-phase 256 x 256 pixels region of interest (ROI) (chosen at random from the 2D BSE cement samples in the NASA PSI database) was converted to a 3-channel representation using the OpenCV library. The extracted feature maps are represented as statistical features

with the aid of Gram matrix, G. During training, the parameters of the generator are optimized by minimizing the loss function defined as:

$$Loss = \sum_{l \varepsilon L} \left\| G^l\left(F^l\left(v_{d,n}\right) - G^l\left(F^l\left(u_d\right)\right)\right)\right\|_f^2 \tag{1}$$

where $\|\cdot\|_f$ is the Frobenius norm, $v_{d,n}$ denotes the solid sections synthesized by the generator, and $u_{d,n}$ is the 2D BSE exemplar. The subscripts d and n correspond to orthogonal direction and slice, respectively. The microstructure reconstruction follows by reducing the loss between the statistical features of the generated slices and the 2D exemplars.

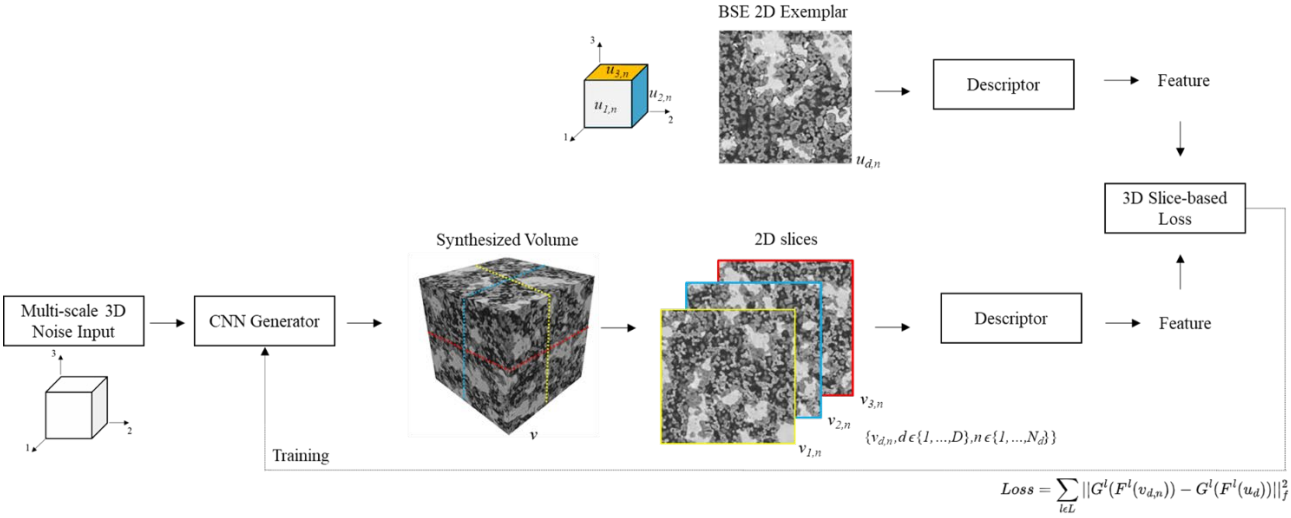

Fig 7. CNN-based deep learning framework to generate 3D microstructure of C_3S samples following the solid texture synthesis approach [17, 19].

C. Reconstructed C_3S Samples and Loss function

The reconstructed 3D microstructures of both 1g and μg samples using the CNN-based deep learning framework are presented in **Figure 8.** The mid-slices of the reconstructed RUCs indicate the influence of the exemplar utilized. The variation in mechanical properties between the reconstructed sub-volumes will be obtained later using a triply-periodic analysis in the NASMAT code. The rate of convergence for both samples was consistent; convergence was achieved after ~1000 iterations (loss function plot, see **Figure 9**). The difference in the converged value between the 1g and μg samples may be attributed to the variation in the statistical features between these samples. The robustness of the algorithm can be noted by the fact that the three orthogonal mid-slices (see the right columns of **Figure 8**) are different for the given 2D BSE exemplar.

The 2D exemplars (256 x 256 pixels; with a resolution of 0.54 μm/pixel, see **Figure 8**) show a notable difference in phase composition in each image. For the 1g samples, the CH crystals are more frequently distributed throughout the C-S-H matrix which has been captured in the reconstructed sub-volumes. The plate-like morphology of the CH crystals, distinct from the μg samples is not that evident in the reconstructed sub-volumes. During the ROI selection, a window of 256 x 256 pixels was chosen from the PSI database that contained elongated CH crystals. As can be seen from **Figure 1(b)** and **Figure 5**, a certain minimum edge length (thereby homogenized volume) is required to best represent the μg samples. Currently, efforts are underway to ascertain this minimum edge length (and homogenization volume) with the aid of micro-CT observations. Moreover, micro-CT data will also enable direct comparison of reconstructed sub-volumes to be utilized as RUCs in the NASMAT code.

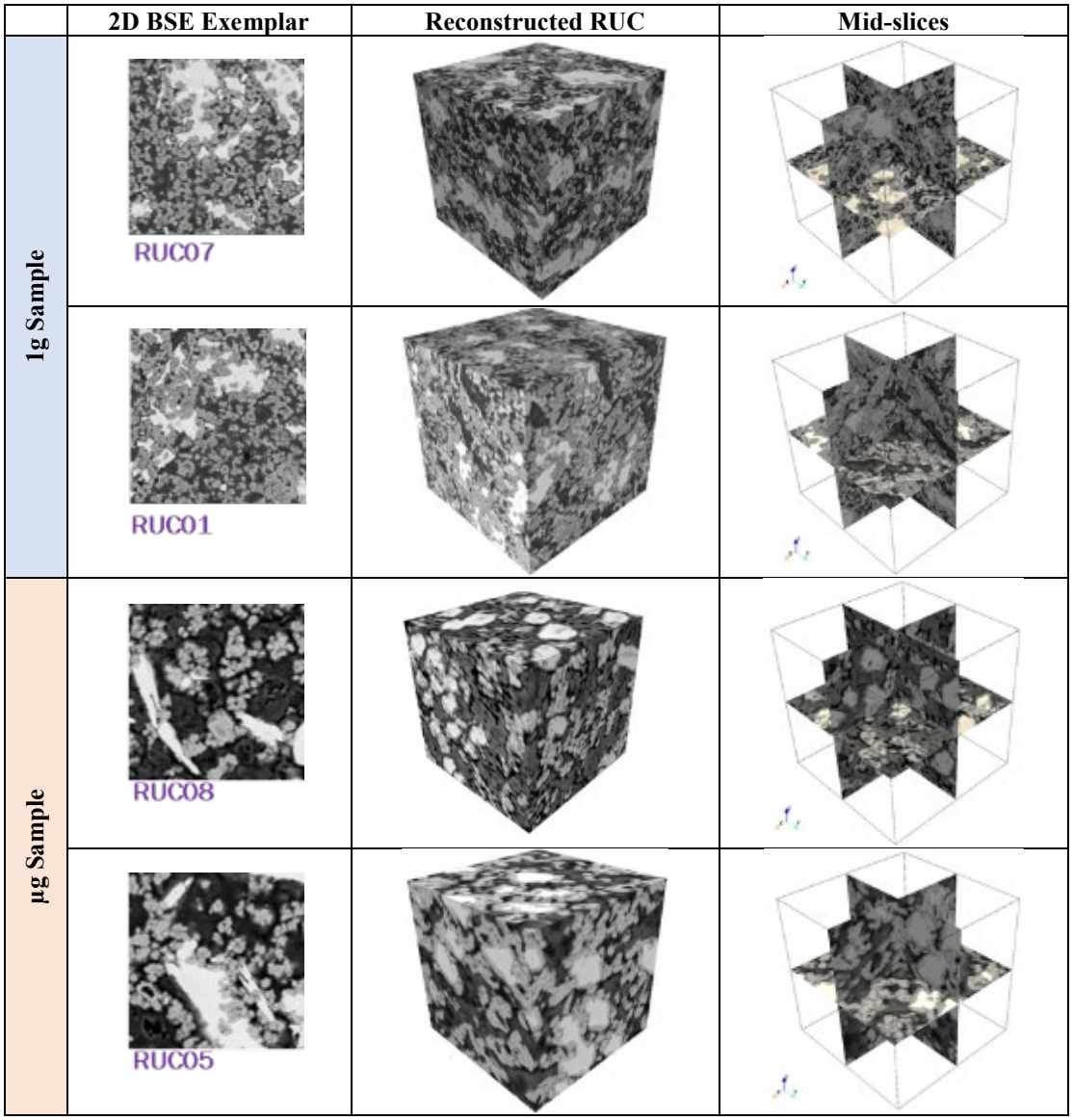

Fig 8. Reconstructed 3D RUCs from 2D BSE exemplars (sigma filtered, 256 x 256 pixels) of C_3S samples (1*g* and μ*g*) using the CNN-based deep learning framework. The white phase corresponds with CH crystals, gray corresponds with the C-S-H matrix and the dark phase corresponds with porosity.

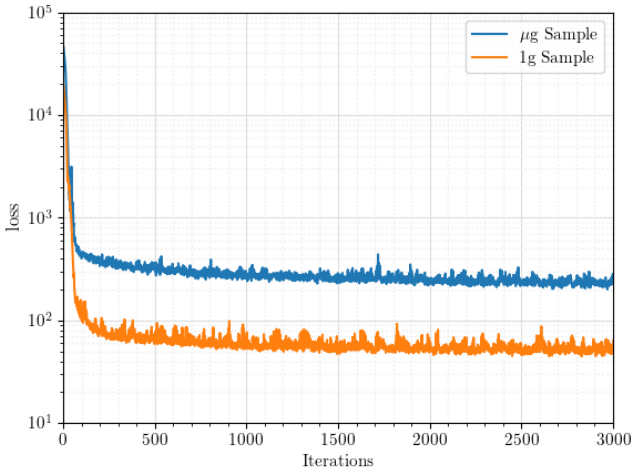

Fig 9. Loss function for the reconstructed 1*g* and μ*g* RUCs.

C. Greyscale-based Thresholding and Phase Allocation in Reconstructed RUCs

Prior to employing the reconstructed RUCs presented in the previous section in the NASMAT code, individual phases must be distinguished, and appropriate constituent material assigned. The previously conducted image segmentation (refer to section II) benchmarked against experimentally measured porosity was utilized. Furthermore, by discerning the phases in the reconstruction sub-volumes, individual phase composition can be obtained and compared against the values obtained from the image analysis. A similar greyscale thresholding approach (overflow method for the porosity/CSH boundary and local minima for the CSH/CH boundary) was used to assign phases in each voxel of the reconstructed 3D RUCs. The identified greyscale-based bounds are provided in the plot (see **Figure 10**). Based on the identified thresholds, the phase-assigned 3D RUCs (porosity, C-S-H matrix, and CH crystals) are shown in **Figure 11.** In general, the deep learning-based reconstruction strategy as exemplified before [19], was able to capture the microstructure in both 1*g* and μ*g* samples. The percentage composition of each phase is also tabulated and compared against image analysis in **Table 2**. The triply-periodic RUCs, with each voxel corresponding to subcell that is assigned to a particular phase, may now be directly utilized in the NASMAT code.

The uniform distribution of CH crystals, characteristic of 1*g* sample was captured well in the reconstructed sub-volumes. In the reconstructed 1*g* sample, the CH crystal composition varied between 8 – 17.40 % compared to 11.3 % obtained from the image analysis. The porosity varied 49 – 52 %, whilst the C-S-H matrix composition was estimated to be 34 – 40 % in the reconstructed RUCs of the 1*g* sample. The spatial distribution of both porosity and CH crystal qualitatively affirms the individual phase distribution found on C_3S samples hydrated on the ground.

In the reconstructed space sub-volumes, the porosity ranged between 57 – 77 %. This range lies within the recorded porosity content using both MIP and image analysis for μ*g* samples. On the other hand, the CH crystal composition was within the range of 4 – 12.30 %. A significant difference to be noted is the non-frequent distribution of the CH crystals in space. However, the elongated plate-like structure is captured in only one of the reconstructed sub-volumes. It confirms the observation that the chosen BSE exemplar governs the ability of the deep learning algorithm to reliably reconstruct the microstructures. Additionally, a minimum homogenized volume must be identified to best represent the CH morphology formed in the microgravity environment. The micro-CT study will be able to shed light on that line and will be used to select exemplars with a minimum edge length. Further studies using low-order probability distribution functions such as the two-point correlation function and lineal-path function will also help evaluate the spatial variation of each reconstructed sub-volume. A note is made here regarding the robustness of the reconstruction algorithm. In general, the statistical features for sub-volume reconstruction are obtained from the input BSE exemplar. Currently, the chosen image size [256 x 256 pixels; resolution = 0.53 μm] does not accurately represent the CH crystal morphology of the μ*g* sample. However, in the case of 1*g* samples, the current implementation shows reasonable accuracy. Future work will include scaling up this technique to be capable of accepting exemplars with increased size [e.g. 1024x1024 pixels]. In addition, a cyclic scheduler to increase the training rate will also be incorporated.

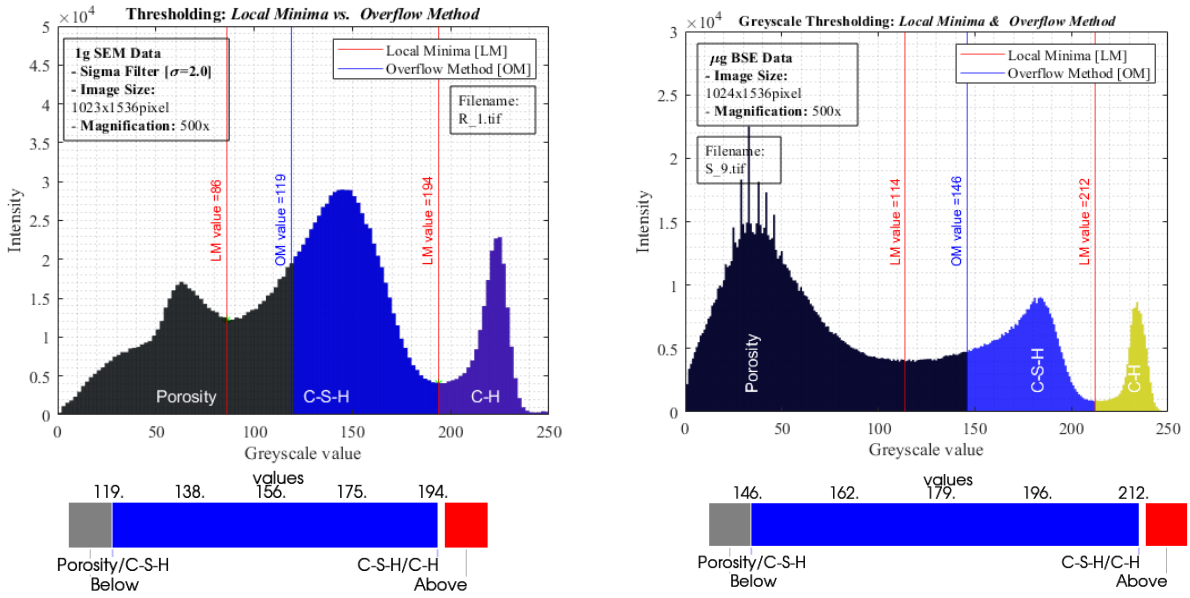

Fig 10. Greyscale thresholding (overflow and local minima approach) of voxels in the reconstructed 3D RUCs of (a) 1*g* and (b) μ*g* C_3S samples.

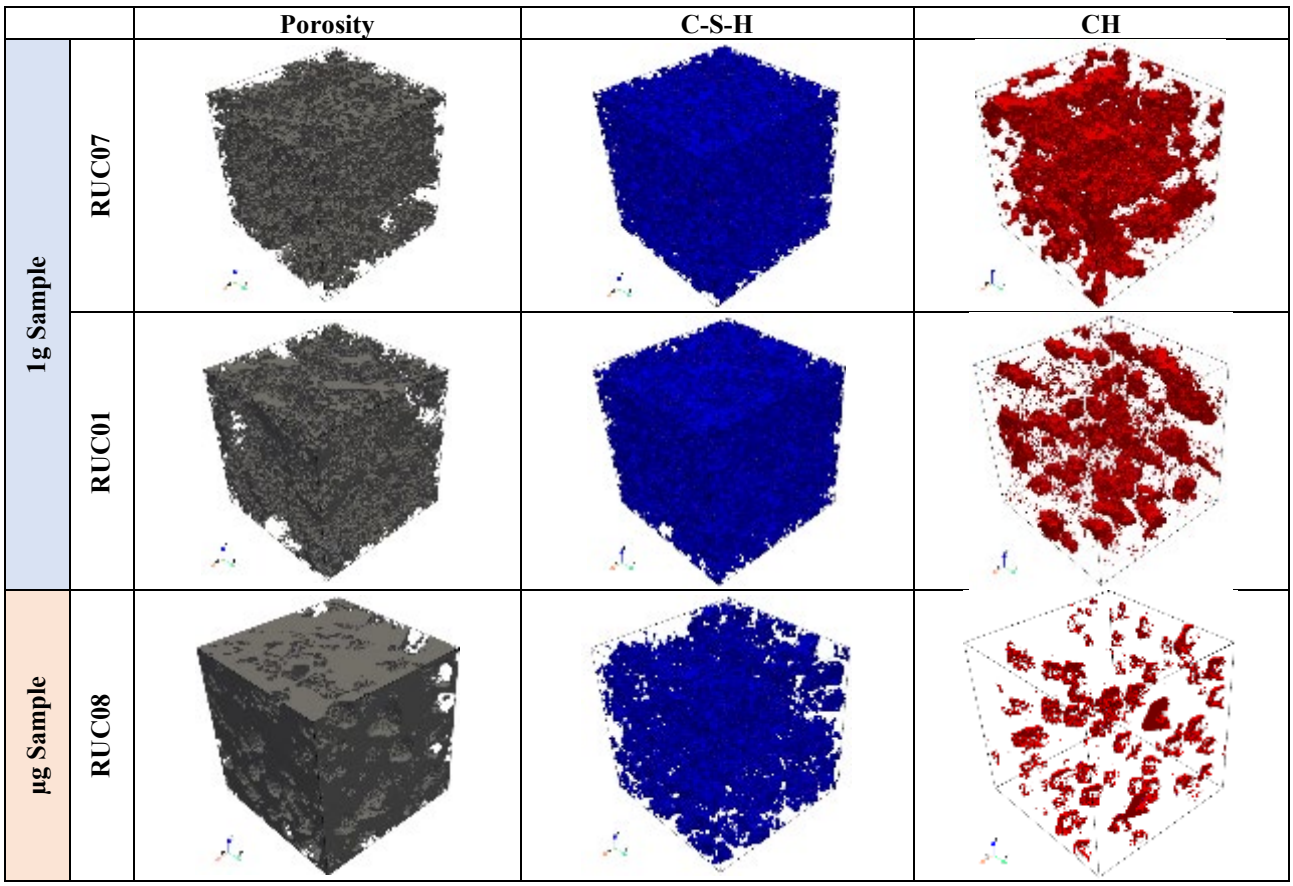

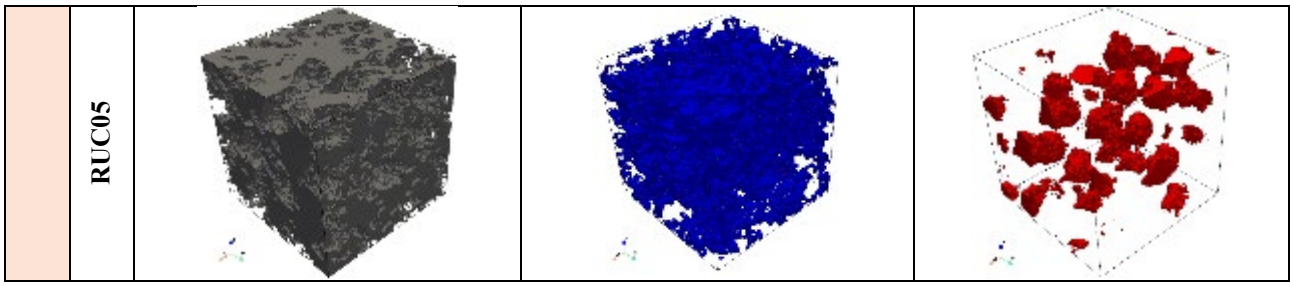

Fig 11. Phase composition in reconstructed 1*g* and µ*g* RUCs [voxel size: 256 pixels] using the CNN-based deep learning framework.

Table 2. Comparison of individual phase composition in reconstructed RUCs and image analysis.

	Porosity	C-S-H	CH
1g Samples – Image Analysis	47.0 % ± 14.2 %	41.6 % ± 12.0 %	11.3 % ± 2.8 %
1g Samples – MIP	48.4 %	-	-
1g Reconstructed RUCs	49.30 % 51.80 %	33.90 % 40.30 %	17.40 % 8.30 %
µg Samples – Image Analysis	70.3 % ± 1.4 %	21.2 % ± 1.2 %	8.5 % ± 1.4 %
µg Samples – MIP	69.4 %	-	-
µg - Reconstructed RUCs	57.30 % 77.40 %	18.80 % 30.40 %	3.90 % 12.30 %

IV. Summary and Future Work

The primary, long-term aim of this study is to perform computational micromechanics analysis of cement binders cured in the microgravity environment to predict the effective mechanical properties and local fields. Due to size limitations and the high porosity content of samples cured in space, conventional mechanical testing is non-viable to ascertain mechanical properties. Initially, the SEM images of both ground and space-returned samples were analyzed to distinguish the individual hydration product. A greyscale-based thresholding approach was used to estimate volume fractions of each phase and porosity; the porosity fraction calculated from this image analysis matched well with the porosity fraction measured using MIP. The phase-segmented 2D BSE image was directly inputted to the NASMAT code as a doubly-periodic RUC and analyzed using HFGMC However, the results were observed to not represent realistic scenario owing to high porosity content, and the inability of the 2D BSE image to accurately capture the 3D microstructure. Hence, 3D microstructures were reconstructed using a deep learning-based solid texture synthesis for both 1*g* and µ*g* samples. The greyscale-based phase segmentation was employed to assign each voxel to a particular phase. The spatial distribution of porosity and portlandite crystals was accurately captured in the 1g sample. However, the distinct plate-like morphology of CH crystals was not captured in the µg sample, due to the choice of ROI. Future work includes the reconstruction of µ*g* sub-volumes using exemplars with a minimum edge length that amply captures the CH morphology. In addition, improvements in the reconstruction code in terms of transfer learning and finding the optimum number of network layers with respect to gram matrix loss will be explored. Finally, the effective properties of the 3D microstructures will be computed through homogenization of triply-periodic RUCs using HFGMC.

Acknowledgments

This research is funded by NASA's Physical Sciences Research Program (80NSSC22K0083). The NASA authors acknowledge support from the NASA Aeronautics Transformational Tools and Technologies Project.

References

[1] Moraes Neves, J., Collins, P. J., Wilkerson, R. P., Grugel, R. N., and Radlińska, A.," Microgravity effect on microstructural development of tri-calcium silicate (C3S) paste," *Frontiers in Materials*, Vol. 83, No. 6, 2019, pp. 1-12. doi: 10.3389/fmats.2019.00083

[2] Collins, P. J., Grugel, R. N., and Radlińska, A., "Hydration of tricalcium aluminate and gypsum pastes on the International Space Station," *Construction and Building Materials*, vol. 285, published online 24 May. 2021. doi: https://doi.org/10.1016/j.conbuildmat.2021.122919

[3] Bednarcyk, B. A., and Arnold, S. M, "MAC/GMC 4.0 User's Manual: Keywords Manual," *No. NAS 1.15: 212077/VOL2*, 2002.

[4] Turner, D.M. and Kalidindi, S.R., 2016. Statistical construction of 3-D microstructures from 2-D exemplars collected on oblique sections. *Acta Materialia*, *102*, pp.136-148.

[5] Sundararaghavan, Veera. "Reconstruction of three-dimensional anisotropic microstructures from two-dimensional micrographs imaged on orthogonal planes." *Integrating Materials and Manufacturing Innovation* 3, no. 1 (2014): 240-250.

[6] Bentz, Dale P. "Three-dimensional computer simulation of Portland cement hydration and microstructure development." *J. Am. Ceram. Soc.* 80, no. 1 (1997): 3-21.

[7] Bullard, Jeffrey W. "A determination of hydration mechanisms for tricalcium silicate using a kinetic cellular automaton model." *Journal of the American Ceramic Society* 91, no. 7 (2008): 2088-2097.

[8] Ye, G., K. Van Breugel, and A. L. A. Fraaij. "Three-dimensional microstructure analysis of numerically simulated cementitious materials." *Cement and Concrete Research* 33, no. 2 (2003): 215-222.

[9] Bishnoi, Shashank, and Karen L. Scrivener. "μic: A new platform for modelling the hydration of cements." *Cement and concrete research* 39, no. 4 (2009): 266-274.

[10] Gutierrez, Jorge, Julien Rabin, Bruno Galerne, and Thomas Hurtut. "On demand solid texture synthesis using deep 3d networks." In *Computer Graphics Forum*, vol. 39, no. 1, pp. 511-530. 2020.

[11] Lee, Jong-Sen. "Digital image smoothing and the sigma filter." *Computer vision, graphics, and image processing* 24, no. 2 (1983): 255-269.

[12] Brand, Alexander S., and Jeffery R. Roesler. "Bonding in cementitious materials with asphalt-coated particles: Part I–The interfacial transition zone." *Construction and Building Materials* 130 (2017): 171-181.

[13] Diamond, S., and J. Huang. "The ITZ in Concrete – A Different View Based on Image Analysis and SEM Observations," Cement and Concrete Composites, Vol. 23, No. 2-3, 2001, pp. 179-188.doi: https://doi.org/10.1016/S0958-9465(00)00065-2

[14] Wong, H. S., M. K. Head, and N. R. Buenfeld. "Pore segmentation of cement-based materials from backscattered electron images." *Cement and concrete research* 36, no. 6 (2006): 1083-1090.

[15 Pietroni, Nico, Paolo Cignoni, Miguel Otaduy, and Roberto Scopigno. "Solid-texture synthesis: a survey." *IEEE Computer graphics and applications* 30, no. 4 (2010): 74-89.

[16] Kopf, Johannes, Chi-Wing Fu, Daniel Cohen-Or, Oliver Deussen, Dani Lischinski, and Tien-Tsin Wong. "Solid texture synthesis from 2d exemplars." *ACM SIGGRAPH 2007 papers*, pp. 2-es. 2007.

[17] Gutierrez, Jorge, Julien Rabin, Bruno Galerne, and Thomas Hurtut. "On demand solid texture synthesis using deep 3d networks." *In Computer Graphics Forum*, vol. 39, no. 1, pp. 511-530. 2020.

[18] Simonyan, Karen, and Andrew Zisserman. "Very deep convolutional networks for large-scale image recognition." arXiv preprint arXiv:1409.1556 (2014).

[19] Zhao, Xin, Xu Wu, Lin Wang, Pengkun Hou, Qinfei Li, Yuxuan Zhang, and Bo Yang. "Three-dimensional Microstructural Image Synthesis from 2D Backscattered Electron Image of Cement Paste." arXiv preprint arXiv:2204.01645 (2022).

[20] Deng, Jia, Wei Dong, Richard Socher, Li-Jia Li, Kai Li, and Li Fei-Fei. "Imagenet: A large-scale hierarchical image database." *2009 IEEE conference on computer vision and pattern recognition*, pp. 248-255. Ieee, 2009.